PNAS RESEARCH ARTICLE | EARTH, ATMOSPHERIC, AND PLANETARY SCIENCES

Shock-formed carbon materials with intergrown sp^3- and sp^2-bonded nanostructured units

Péter Németh[a,1], Hector J. Lancaster[b], Christoph G. Salzmann[c], Kit McColl[d], Zsolt Fogarassy[e], Laurence A. J. Garvie[f], Levente Illés[e], Béla Pécz[e], Mara Murri[g], Furio Corà[c], Rachael L. Smith[c], Mohamed Mezouar[h], Christopher A. Howard[b], and Paul F. McMillan[c]

Edited by Russell Hemley, University of Illinois at Chicago, Chicago, IL; received March 10, 2022; accepted June 14, 2022

Studies of dense carbon materials formed by bolide impacts or produced by laboratory compression provide key information on the high-pressure behavior of carbon and for identifying and designing unique structures for technological applications. However, a major obstacle to studying and designing these materials is an incomplete understanding of their fundamental structures. Here, we report the remarkable structural diversity of cubic/hexagonally (*c*/*h*) stacked diamond and their association with diamond-graphite nanocomposites containing sp^3-/sp^2-bonding patterns, i.e., diaphites, from hard carbon materials formed by shock impact of graphite in the Canyon Diablo iron meteorite. We show evidence for a range of intergrowth types and nanostructures containing unusually short (0.31 nm) graphene spacings and demonstrate that previously neglected or misinterpreted Raman bands can be associated with diaphite structures. Our study provides a structural understanding of the material known as lonsdaleite, previously described as hexagonal diamond, and extends this understanding to other natural and synthetic ultrahard carbon phases. The unique three-dimensional carbon architectures encountered in shock-formed samples can place constraints on the pressure–temperature conditions experienced during an impact and provide exceptional opportunities to engineer the properties of carbon nanocomposite materials and phase assemblages.

shock-formed carbon | diaphite | cubic/hexagonally stacked diamond | ultrahard material

Significance

Diamond is the hardest material found in nature. Its applications range from abrasives and electronics to nanomedicine and laser technology. The common form of diamond is cubic. Yet, dense carbon materials formed by shock compression have been described as hexagonal diamond or lonsdaleite. This study provides a structural understanding of lonsdaleite and demonstrates the existence of bulk materials containing extensive regions of nanostructured diamond and graphene-like intergrowths called diaphites. The structural complexities found in Canyon Diablo iron meteorite diamonds occur in a wide range of carbonaceous materials, and their identification can place constraints on the pressure–temperature conditions experienced during an impact. The predicted advanced properties of such materials highlight their potential use in future engineering applications.

The variable bonding nature of carbon–carbon bonds gives rise to materials with widely different properties ranging from semimetallic graphite to the wide-bandgap insulator diamond. Diamond is the hardest known material formed by sp^3-bonded layers arranged in a cubic stacking arrangement. Another sp^3-bonded allotrope with hexagonal layer stacking was proposed based on additional broad diffraction features reported from samples prepared by static and dynamic compression of graphite (1, 2). Analogous patterns were also observed from hard carbon materials extracted from the Canyon Diablo iron and Goalpara ureilite meteorites (3) and assigned to lonsdaleite (4). This name is also applied to the sp^3-bonded structure type with hexagonal layer stacking; this conflation in nomenclature has resulted in some confusion that must be resolved for a complete understanding of the mineral phase and its material properties. The occurrence of lonsdaleite was used as an indicator of asteroidal impacts (5–7), while experimental and theoretical investigations have indicated it to be superhard and possess other attractive properties that can be competitive with or even superior to those of diamond (8). It is now recognized that these materials can contain an intimate mixture of cubic and hexagonal nanostructured units, along with sp^2-bonded domains, that can lead to tunability of the mechanical and other properties of the nanocomposite structures and modify the interpretation of their formation conditions in natural impact environments (9, 10).

The identification of lonsdaleite in hard carbon-type materials was based on X-ray diffraction (XRD) patterns that show reflections from cubic diamond and broad and poorly resolved maxima at 0.218, 0.193, 0.151, and 0.116 nm that were indexed using a hexagonal unit cell (3, 4). The XRD results were later complemented by transmission electron microscopy (TEM) and electron diffraction results, and by Raman spectroscopic data, leading to the widely accepted conclusion that 1) the pure hexagonal diamond structure had been identified and 2) it was present among natural and synthetic samples (5, 11). However, the recent use of advanced TEM techniques, which achieve atomic-level resolution of the nanostructures, revealed a wide range of sp^3 and sp^2 structures that are bonded together forming a variety of nanocomposite materials (9, 10).

Recent structural studies indicate that lonsdaleite from the Canyon Diablo iron meteorite and other meteoritic samples can be described in terms of faulted and twinned domains of cubic diamond, rather than a discrete phase or structure (12, 13). Salzmann et al. (14) applied the MCDIFFaX technique to quantitatively analyze the XRD profiles of natural and laboratory-produced diamond samples in terms of ordered

Author contributions: P.N., L.A.J.G., and P.F.M. designed research; P.N., H.J.L., C.G.S., K.M., Z.F., L.I., B.P., M. Murri, M. Mezouar, and P.F.M. performed research; P.N., H.J.L., C.G.S., K.M., Z.F., L.A.J.G., B.P., M. Murri, F.C., R.L.S., M. Mezouar, C.A.H., and P.F.M. analyzed data; and P.N. and P.F.M. wrote the paper.

The authors declare no competing interest.

This article is a PNAS Direct Submission.

Copyright © 2022 the Author(s). Published by PNAS. This article is distributed under Creative Commons Attribution-NonCommercial-NoDerivatives License 4.0 (CC BY-NC-ND).

[1]To whom correspondence may be addressed. Email: nemeth.peter@csfk.org.

This article contains supporting information online at http://www.pnas.org/lookup/suppl/doi:10.1073/pnas.2203672119/-/DCSupplemental.

Published July 22, 2022.

Downloaded from https://www.pnas.org by Universita di Milano Bicocca on July 25, 2022 from IP address 149.132.95.191.

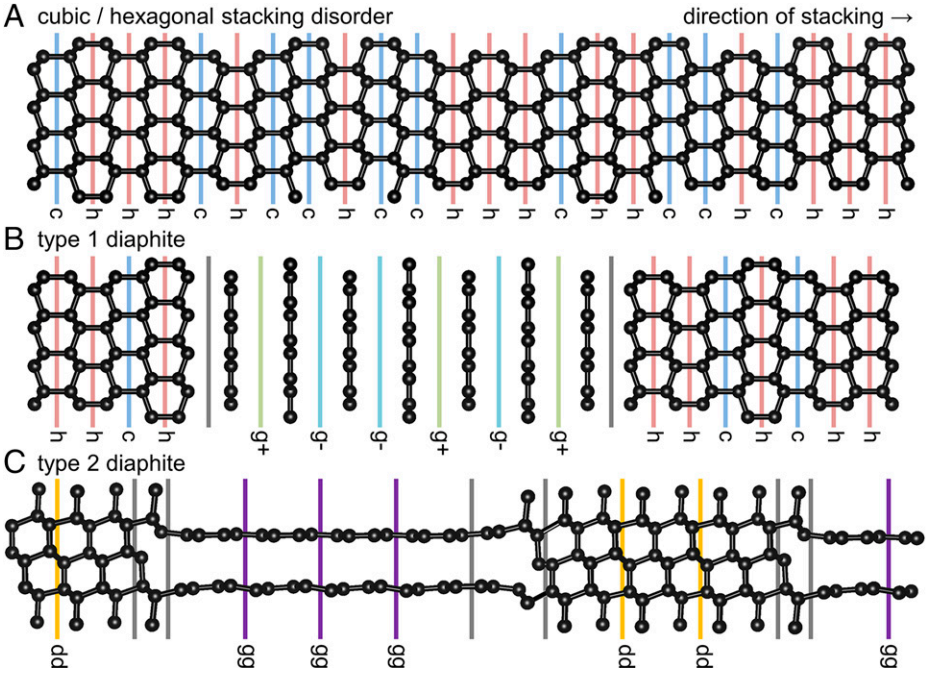

Fig. 1. Structures of disorder types in diamond viewed along <011>. (*A*) Cubic/hexagonal stacking disorder with "c" and "h" denoting cubic and hexagonal stacking, respectively. (*B*) Type 1 diaphite in stacking disordered diamond. Note that for simplicity diamond and graphene surfaces are not reconstructed. The reconstructed interfaces can be found in refs. 9 and 10. The two different types of stacking of the graphene sheets are indicated by "g+" and "g−." A random stacking sequence is shown in *B*. (*C*) Type 2 diaphite in cubic diamond with "dd" and "gg" indicating the stacking of diamond and graphene segments, respectively. Interfacial stacking boundaries between diamond and graphene are shown as gray lines in *B* and *C*.

versus disordered cubic and hexagonal layer stacking arrangements (Fig. 1*A*). The refined stacking probabilities can be plotted on a stackogram that locates the structures within the poles of a diagram between randomly stacked cubic (*c*) to hexagonal (*h*) diamond, versus $(ch)_x$ and a physical mixture of *c* and *h* polytypes. In contrast to recent discussions of hexagonal diamond structures, the MCDIFFaX analyses indicates that no examples of the pure lonsdaleite 2H layer stacking structure have been identified among natural or synthetic samples available to date (14–16) (*SI Appendix, Supplementary Information 1*).

Recent high-resolution TEM (HRTEM) investigations combined with density functional theory (DFT) structure modeling of impact- and laboratory-produced carbon shows the presence of graphitic layers inserted within and coherently bonded at specific angles to the sp^3-bonded matrix (9, 10, 17, 18). These nanostructures are termed "diaphites," similar to the diamond-graphene crystalline layers observed following photoexcitation at graphite surfaces (19, 20). Although these early papers reported two-dimensional (2D) structures (19, 20), the description of diaphite was extended to three-dimensional (3D) structures of crystallographically intergrown diamond-graphene (9, 10, 17, 18). Here we use the word graphene for a few (1 to 10) graphitic layers and graphite for a larger number of layers. In diaphites the numbers of graphitic and diamond layers are variable, and these complex structures are not simple physical mixtures, but they are characterized by the structurally intergrown layered sp^2- and sp^3-bonded carbon domains on the nanoscale and thus give rise to distinct diffraction features that physical mixtures do not display (9, 10, 17, 18). Two diaphite structure types have been recognized: 1) type 1 diaphite in which few-layered sp^2-bonded graphene layers are inserted between {111} surfaces of diamond (Fig. 1*B*) and 2) type 2 diaphite in which the graphene layers are coherently bonded at high angles with the {113} diamond surfaces (Fig. 1*C*). In addition to shock-formed samples (9, 10, 18), diaphite has also been reported from meteoritic nanodiamonds and thosed produced by chemical vapor deposition (17). Recently, researchers proposed another graphene-diamond structure called gradia (21–24), which in contrast to diaphite lacks a definitive epitaxial relationship. Such gradia structures have been recognized from static high-pressure (HP) and high-temperature (HT) compression of graphite (21) as well as HP and HT treatment of multiwall carbon nanotubes (25) and fullerenes (26). The mixed hybridized bonding in diaphite and gradia structures contributes further to determining the mechanical and thermal relaxation properties as well as the structural transformation pathways encountered during compression and decompression events from initially graphitic to diamond-related phases, while resulting in unique low-dimensional electronic conductivity and superconductivity at the sp^3/sp^2 interface within the otherwise insulating material (9, 10, 17, 24). Such mixed hybridized bonding can also be responsible for the unique low-dimensional structures of carbon nanothreads that are being developed as high-strength nanomaterials with tunable electronic and chemical properties (24, 27).

In the present work we show that both types of diaphite are abundant within the hard carbon grains from the Canyon Diablo iron meteorite (*SI Appendix*, Table S1 and Fig. S1). These grains represent the type of material used to establish lonsdaleite as a mineral (4). We investigate the graphite occurring both in massive form and as aggregates of particles with cuboid morphology known as cliftonite (28, 29). Many of the carbon grains, including those with cuboid morphology, exhibit high chemical resistance and extreme hardness, leading to their designation as "diamonds". Evidence suggests these "diamonds" formed by shock compression of the initial graphite (30–33). Using HRTEM and synchrotron microbeam XRD mapping as well as multiwavelength Raman spectroscopy and mapping, we reveal the structural complexity of the "diamonds" from the Canyon Diablo meteorite and extend this understanding to other carbonaceous materials produced by shock and static

Downloaded from https://www.pnas.org by Universita di Milano Bicocca on July 25, 2022 from IP address 149.132.95.191.

compression or by deposition from the vapor phase. The recognition of the sp^3/sp^2 intergrowths within the hard carbon grains formed by shock compression from graphite places constraints on the pressure–temperature conditions experienced during the impact event and may suggest strategies to engineer these carbon nanocomposite structures with unique and potentially useful mechanical and electronic properties (9, 10, 24, 26, 34, 35).

Results

Diversity and Complexity of Nanocomposite *c/h* Stacked Diamond and Diaphite Structures. From 100 Canyon Diablo carbon grains, 4 representative (grains 2, 6, 7, and 8) (*SI Appendix*, Fig. S1 and Table S1) were selected for detailed investigation. Grain 2 is mechanically soft and similar to graphite. Grains 7 and 8 exhibit extreme hardness akin to diamond, whereas grain 6 shows mechanical polishing properties intermediate between grains 2 and 7. The synchrotron microbeam XRD maps of these grains reveal a diversity of structures on a micrometer to submicrometer scale, including mixtures of *c/h* layer stacking disordered diamond, graphite, and type 1 and type 2 diaphites (Fig. 2). These composite structures, confirmed by TEM investigations, are evidenced by the strong diffuse X-ray scattering, which does not occur for physical mixtures (14). The XRD patterns from the mechanically soft grain 2 are dominated by graphite, whereas the patterns from grains 7 and 8 are dominated by sp^3-bonded structures. Grain 6 shows the presence of abundant sp^2-graphitic layered structures. The 2D XRD patterns from grains 6, 7, and 8 show diffuse and continuous rings, indicating their nanocrystalline nature (Fig. 2*A*). Four main diffraction rings,

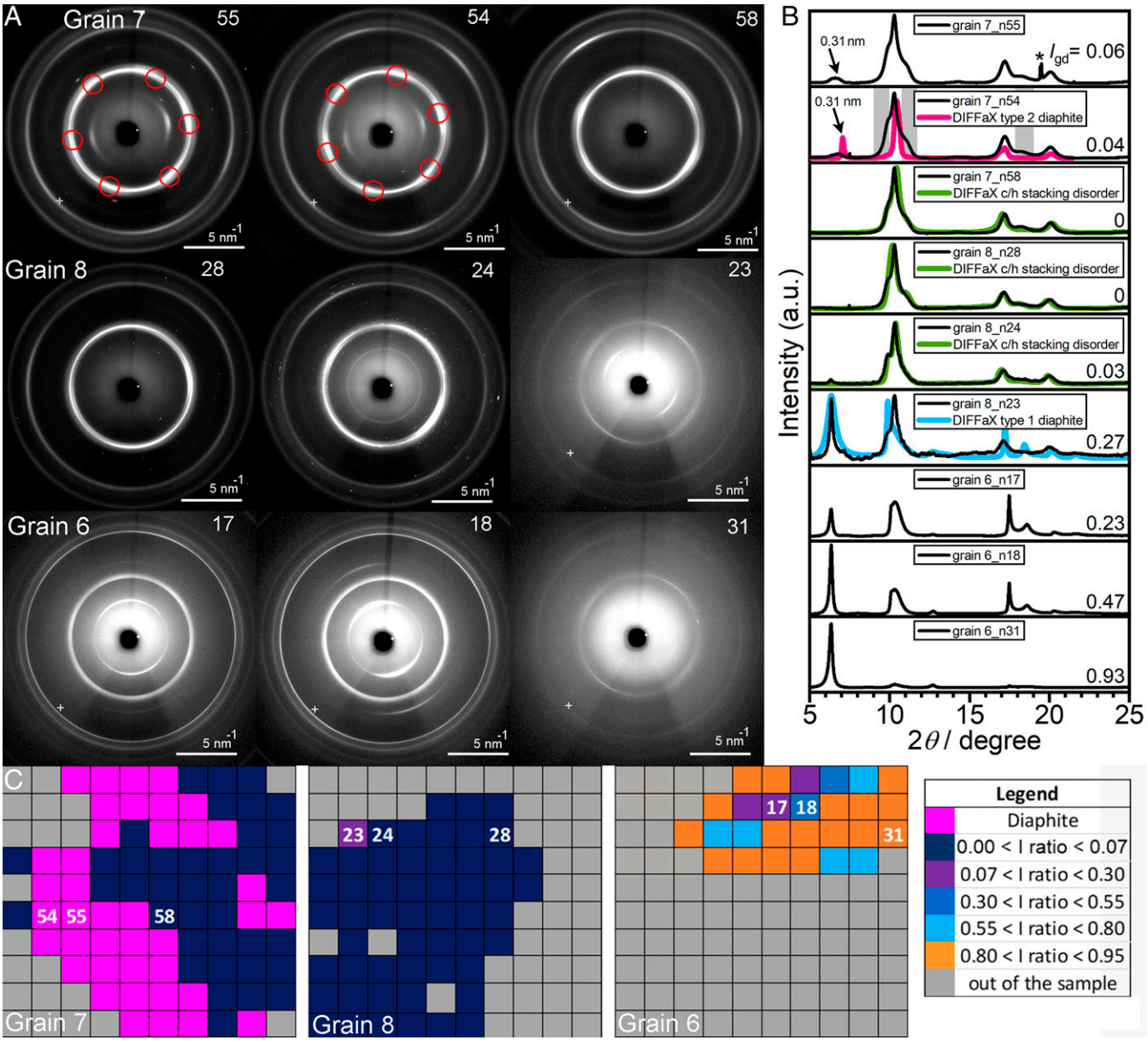

Fig. 2. Synchrotron XRD data (λ = 0.03738 nm) of heterogeneous structures within Canyon Diablo hard carbon grains. (*A*) Selected 2D XRD patterns obtained from 2-μm^2-areas and (*B*) their corresponding one-dimensional intensity profiles. These profiles display variability between fully sp^2-bonded and sp^3-bonded structures. Red circles in *A* mark hexagonally arranged features. Black arrows on patterns 54 and 55 mark the 0.31-nm d-spacing arising from compressed graphene layers of type 2 diaphite. The asymmetric and broad peaks indicate stacking disordered diamond and intimately intergrown diaphite structures. The simulated patterns using *c/h* stacking disorder, type 1 ($\Phi_c = \Phi_h = 0.4$, $\Phi_{dg} = \Phi_{gd} = 0.2$, $\Phi_{g+} = \Phi_{g-} = 0.4$) and type 2 diaphite ($\Phi_{gg} = 0.9$, $\Phi_{dg} = 0.0053$, $\Phi_g = 0.1$) are shown in green, blue, and pink, respectively. The cubicities, Φ_c, for the *c/h* stacking disordered samples are noted in the figure together with the I_{gd} peak intensity ratios [$I_{gd} = I_{sp2}/(I_{sp2} + I_{sp3})$]. The asterisk indicates an impurity peak. (*C*) Color-coded XRD maps (*Right*) corresponding to heterogeneous structures of selected grains (a pixel covers a 2-μm^2 area). The I_{gd} ratios are reported in *SI Appendix*, Table S2. Regions with intensity ratios >0.01 are marked as diaphite (pink).

Downloaded from https://www.pnas.org by Universita di Milano Bicocca on July 25, 2022 from IP address 149.132.95.191.

centered at ~7°, ~12°, ~17.5°, and ~20° 2θ (λ = 0.03738 nm) can be recognized, corresponding to 0.334- (reduced to 0.31 nm in some areas), 0.21-, 0.125-, and 0.105-nm spacings. The first ring, which is characteristic for graphite and is also expected for diaphite nanostructures, is absent from some areas of grains 7 and 8. The diffraction rings are broad with the highest intensity circles extending across several pixels. Most XRD patterns from grains 7 and 8 show asymmetric splitting and exceptional width for the second ring centered at ~12° 2θ (d spacing of ~0.21 nm), corresponding to the (111) planes of diamond, and the intensity distribution around the rings show quasi-sixfold symmetry (Fig. 2*A*). Integrating the intensity of the wide rings from the 2D patterns gives broad and asymmetric XRD peaks (Fig. 2*B*). This asymmetry and diffuse scattering are particularly apparent for the peak centered at ~12° 2θ consistent with stacking disordered *c/h* diamond (14–16). The cubicity indices [switching probability calculated according to $\Phi_c = \Phi_{hc}/(\Phi_{hc} + \Phi_{ch})$] of three samples from grains 7 and 8 are in the 0.5752 to 0.6308 range (Fig. 2*B*), which indicates substantial hexagonal diamond stacking.

Several patterns show an intense sharp peak near 6.5° 2θ (d spacing of 0.34 nm), corresponding to graphite or multilayered graphene units, which likely arise from type 1 diaphite (9). In cases for which the diffraction pattern is dominated by stacking disordered *c/h* diamond, a broadened feature is also present at slightly higher 2θ values, corresponding to graphitic structures with a smaller interlayer spacing. These features indicate the presence of type 2 diaphite in which the graphitic layers are coherently bonded at high angles within the surrounding *c/h* stacking disordered diamond (9, 10). For several patterns, this broad peak is positioned at 0.31 nm instead of 0.334 nm, which is consistent with the occurrence of type 2 diaphite in which the interlayer spacings are compressed by the necessity of coherent bonding between the edges of the graphene layers and the {113} diamond surfaces (9, 10). The broadness of the peak is likely to be due to a slight variation in interlayer spacing for the graphene layers depending on the size of the graphene/diamond domains, a feature also observed in our computational models. Such interlayer spacings have been reported from the quenched material obtained following HP–HT treatment of graphite (21) and fullerenes (26).

The diversity of possible structures and resulting diffraction data represent a challenge for quantifying the XRD patterns. Due to the identical direction of stacking, *c/h* stacking disorder can be combined with type 1 diaphite structures in DIFFaX, allowing modeling of nanocomposite structures containing *c/h* sp^3-bonded stacking and few- to multilayered graphene units as found in type 1 diaphite (9). However, for type 2 diaphite the direction of stacking differs between the two structural motifs, and hence it was only possible to interlace cubic diamond with graphene segments, as explained in *SI Appendix, Supplementary Information 2* and Fig. S2. Simulated diffraction patterns representing the three types of structural disorder are shown in Fig. 2*B* along with the experimental data.

In order to obtain an estimate of the sp^2/sp^3 carbon content across the samples and averaged over their depth profiles, we calculated the I_{gd} intensity ratios of the diffraction features at ~6° and 10° 2θ (Fig. 2*B* and *SI Appendix*, Table S2). This simplified quantification demonstrates that in addition to the diversity of *c/h* stacked diamond and diaphite nanostructures significant spatial variability of the sp^3/sp^2 carbon content occurs within our samples (Fig. 2*C*).

Intergrowth among *c/h* Stacked Diamond and Type 1 and Type 2 Diaphite Nanostructural Units. Focused ion beam (FIB) lamellae reveal the atomic-scale structure of the mechanically soft (grain 2), intermediate (grain 6), and ultrahard (grain 7) samples. Consistent with our XRD results, the TEM investigations show that grain 2 is dominated by 100- to 500-nm-wide bundles of relatively well-ordered 3R graphite (*SI Appendix*, Fig. S3). Such bundles with similar sizes are also locally present in grains 6 and 7 (Fig. 3), but their structures are more complex. The HRTEM images of grain 6 show type 1 diaphite within domains dominated by poorly ordered 3R-stacked graphite (Fig. 3*A*). This composite structure is characterized by the intergrowth of <011> projected diamond and <01–10> projected graphite (Figs. 3*B* and *C* and 4*A*–*C*). The diamond units are small (~1 to 2 nm) and distributed throughout the graphite (Fig. 3*C*). The lateral terminations of the diamond and graphite units give rise to type 2 diaphite (Fig. 4*B* and *C*). According to DFT calculations (9, 10), this structure should contain compressed graphene (0.31 nm) layers at the interface along <110> diamond projection. However, the thickness of the FIB sample (~50 nm) and the superposition of overlapping structures make the 0.31-nm spacing measurement unreliable at the interface from the experimental HRTEM images (Fig. 4*B*); only regular graphene spacings (~0.34 nm) can be reliably determined. TEM investigation of the hard carbon grain 7, which is covered by a 50- to 100-nm-thick graphitic coating (*SI Appendix*, Fig. S4), exemplifies the nanoscale complexity of the disordered diamond and diaphite intergrowths. Low-magnification TEM imaging reveals an ~100-nm feathery texture (Fig. 3*D*), which could be associated with previous graphitic layering arranged into bundles, similar to those found in grain 6 (Fig. 3*A*). The HRTEM images reveal the complexity of {111} stacking faults (Fig. 3*E*), reported previously in ref. 12, as well as their intrinsic association with type 1 diaphite (Fig. 3*F*). These images and the continuous streaking of 111 diamond reflections on the fast Fourier transforms (FFTs) indicate that regions of ordered diamond and diaphite are below the nanometer scale.

The texture of the hard carbon was also studied by rotating grain 7 by 90°, i.e., in an approximately <121> diamond orientation (Fig. 3*G*). The bundle texture, i.e., the ~100- to 300-nm-thick layering, appears on dark-field images taken by selecting graphite- and diamond-type diffraction features (*SI Appendix*, Fig. S5) but is absent on the bright-field images (Fig. 3*G*). Although the selected-area electron diffraction (SAED) pattern shows continuous rings, the intensity distribution around the 111 diamond spots reveals a quasi-sixfold symmetry (Fig. 3*G*). The HRTEM images reveal 5-to-10-nm-sized regions exhibiting hexagonal fringes with a 0.21-nm spacing (Figs. 3*H* and 4*D* and *E* and *SI Appendix*, Fig. S6*A*). We attribute this sixfold symmetry to type 2 diaphite (9, 10, 17). Since such regions are nanosized (9, 17), the interface of type 2 diaphite, i.e., <121> diamond and <0001> graphite units, is only visible for vertically aligned structures (Fig. 4*D*–*F*). However, for vertically misaligned structures the identification of these unit in the 50- to 60-nm-thick FIB lamella is challenging. Regions displaying distorted 12-fold rotational symmetry also occur (*SI Appendix*, Fig. S6*B*), which can be associated with the rotation of stacked graphene units in type 2 diaphite nanostructures (17).

The regions displaying quasi-sixfold symmetry are continuous with fringes displaying 0.320- to 0.334-nm spacings (Figs. 3*H* and 4 *G*–*I* and *SI Appendix*, Fig. S7). The 0.320-nm spacing, observed also in our XRD data (Fig. 2*B*), is consistent with the compressed graphene layers occurring within type 2 diaphite in its side view (<110> diamond and <01–10> graphite) projection (Fig. 3*I*). The slightly larger d-spacing (0.320 nm) measured experimentally compared to the DFT-based structure

Downloaded from https://www.pnas.org by Universita di Milano Bicocca on July 25, 2022 from IP address 149.132.95.191.

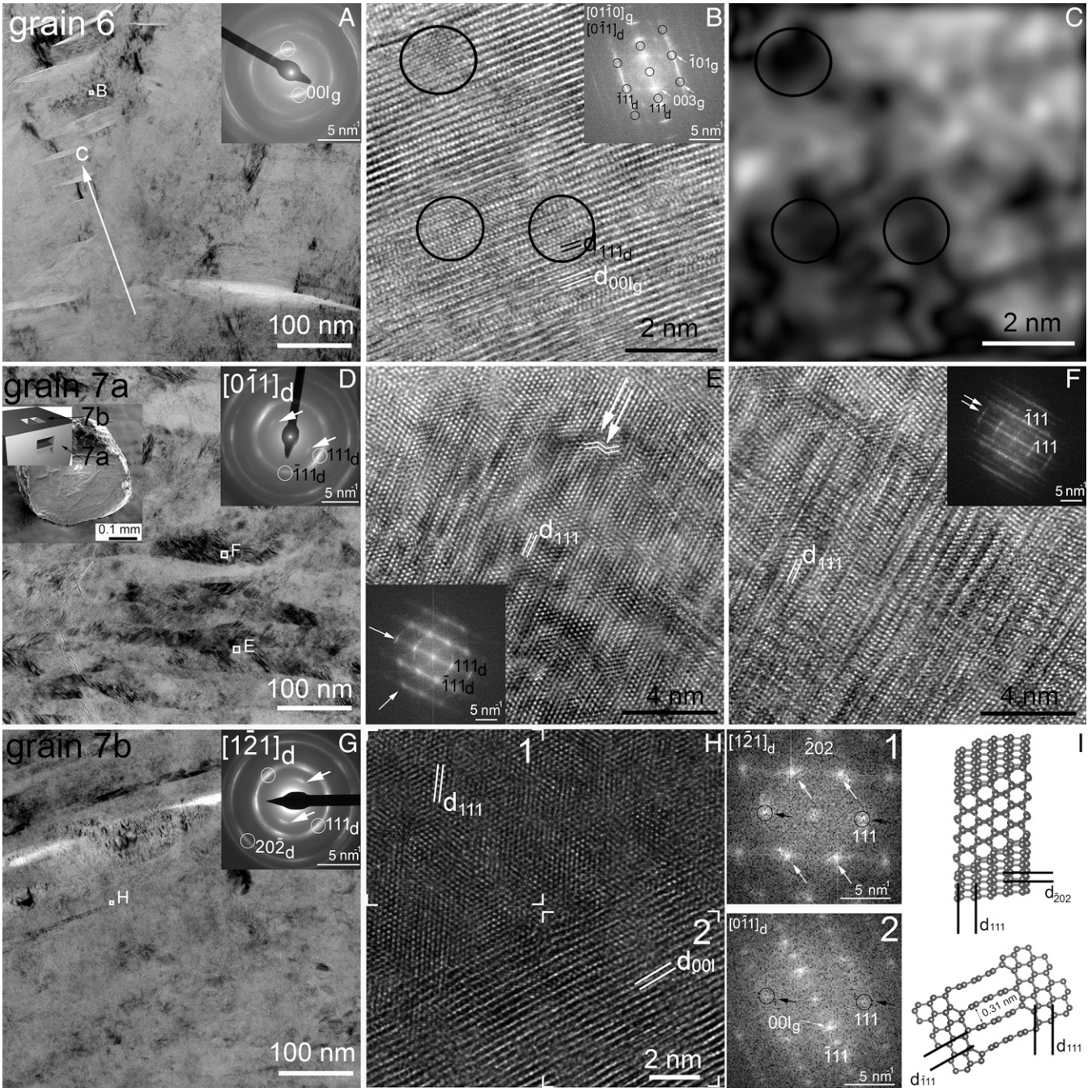

Fig. 3. Diaphite structures from Canyon Diablo hard carbon grains. (*A*) Bright-field TEM (BFTEM) image and SAED pattern from grain 6. White circles mark 00l graphite reflections. (*B*) HRTEM image and its FFT taken from the circled area B in *A* showing type 1 diaphite. Black circles mark diamond and white arrows point to 3R graphite reflections. The FFT resembles the diffraction features and the crystallographic relationship that was published in refs. 9 and 49. (*C*) Amplitude image calculated from the 003 set of 3R graphite reflections from the FFT. Black areas indicate diamond-rich regions within type 1 diaphite. (*D*) BFTEM image of the FIB lamella 7a and its SAED pattern. White circles mark diamond and white arrows point to graphite 00l reflections, respectively. SEM image of grain 7 and the orientations of the two perpendicular FIB lamella (7a and 7b) are inserted. (*E*) Abundant {111} stacking faults (white arrows). (*F*) {111} stacking faults intimately intergrown with type 1 diaphite from thick (~50 nm) areas give rise to complexity and streaking of diffraction spots (white arrows). (*G*) BFTEM image of the FIB lamella 7b. (*H*) Hexagonal features and shortened graphene spacings (*SI Appendix*, Fig. S7) indicating intergrowth between two projections of type 2 diaphite. (*I*) FFTs of selected regions in *H* and the structure models of type 2 diaphite. White arrows point to hexagonally arranged reflections for 1. Black circles and arrows for 1 and 2 mark coinciding 111 diamond reflections of the two diaphite projections.

model (0.31 nm) can be explained by the imperfect orientation of the lamella. The front and side view projected type 2 diaphite domains are not only adjacent to each other but they are crystallographically intergrown (Figs. 3*I* and 4 *H* and *I*). Furthermore, the compressed graphene occurring within type 2 diaphite is also intergrown with bulk (i.e., noncompressed) graphene layers. We note that the <011> diamond projection in the lateral extent of these regions matches that of type 1 diaphite, which suggests that type 2 and type 1 diaphites are also intergrown on the nanometer scale (Figs. 3*I* and 4 *H* and *I*).

Raman Signatures of *c/h* Stacked Diamond and Diaphite Nanostructures. Raman spectroscopy is used extensively to characterize the structures of carbon materials (5, 36–39). Using this technique to analyze mixtures of sp^3- and sp^2-bonded materials represents a significant challenge due to the markedly different

Downloaded from https://www.pnas.org by Universita di Milano Bicocca on July 25, 2022 from IP address 149.132.95.191.

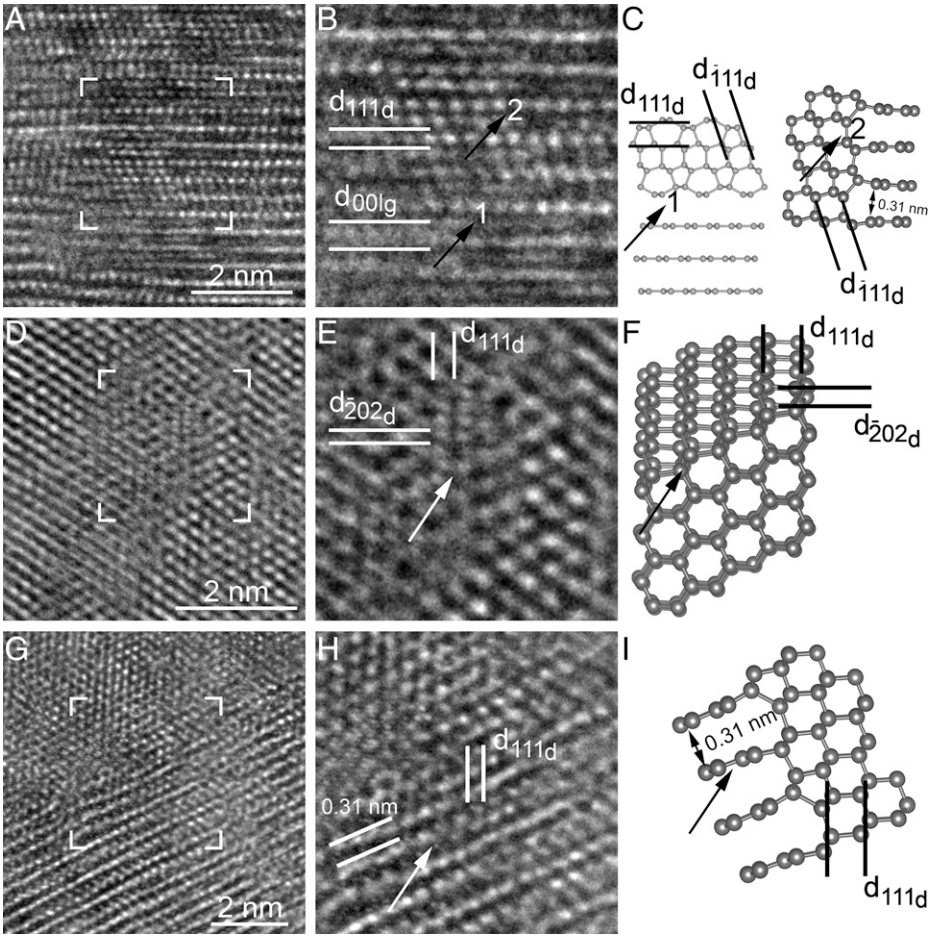

Fig. 4. Magnified view of the interface structures of type 1 and type 2 diaphites. (*A*) HRTEM image from grain 6. (*B*) Magnified region showing type 1 and type 2 diaphite interfaces (marked by black arrows). (*C*) Structure models of type 1 and type 2 diaphites along $<110>_d$ projections. (*D*) HRTEM image from grain 7b. (*E*) Magnified region showing type 2 diaphite interface. Structure model of the interface along the $<121>_d$ projection. (*G*) HRTEM image from grain 7b. (*H*) Magnified region showing the type 2 diaphite interface along the $<110>_d$ projection and (*I*) the corresponding structure model of the interface.

electronic properties of these structures. Diamond shows a single sharp Raman peak at 1,332 cm^{-1} that broadens, shifts to lower wavenumber, and becomes asymmetric for crystallites <10 nm (40). Although the experimental spectrum of pure hexagonal diamond is unknown, DFT calculations predict a main peak at 1,305 cm^{-1} with less-intense peaks near 1,244 and 1,356 cm^{-1} (15, 41). Calculated spectra of diamonds with *c/h* randomly stacked layers show evolution between these end member predictions as a function of cubicity index, modified by the presence of ordering among the stacked layers (16).

Graphite exhibits a single sharp Raman peak at 1,575 to 1,580 cm^{-1}, arising from the in-plane stretching of the aromatic C–C rings. As the structure becomes disordered this peak becomes broadened and asymmetric and moves to a higher wavenumber, while a second broad band occurs near 1,355 cm^{-1} that increases in intensity with increasing disorder within the layered structure. These two features are referred to as the "G" and "D" bands, respectively. The D-peak frequency and I_D/I_G intensity ratio increase systematically with excitation energy (42). These effects have been calibrated against the degree of structural disorder related to layer domain size and buckling, interlayer spacing, and atomic defects.

The first-order Raman spectrum of graphene shows G and D features that vary in position, shape, and relative intensity as a function of the number of graphitic planes and excitation wavelength. Significant changes are noted in the second-order bands due to overtones and combinations involving the D features, which become a significant marker for determining the number of layers in few-layered graphene (43). The analysis of samples containing both sp^3 and sp^2 structures is further complicated by the fact that the intrinsic intensity of the main Raman features for sp^3-bonded phases are lowered by a factor of 10^2 to 10^3 compared with those for graphitic structures (38) (*SI Appendix*, Fig. S8).

We investigated grains 2, 6, 7, and 8 using multiwavelength Raman spectroscopy and mapping (Fig. 5*A* and *SI Appendix*, *Supplementary Information 3*). Surprisingly, although the XRD and TEM data indicated that the high hardness grains 7 and 8 are dominated by sp^3-bonded structures, their Raman spectra most closely resemble the features of graphitic materials. The G peaks near 1,580 to 1,590 cm^{-1} are associated with sp^2 bonding, while the more intense peak at 1,315 to 1,335 cm^{-1} could be interpreted as the D feature of disordered graphite. The D band exhibits significant dispersion and width as a function of laser excitation wavelength, with an additional shoulder present for some samples (Fig. 5*B*). A sharp peak at 1,332 cm^{-1} occurs in several spectra from grain 8, indicating the presence of well-crystallized cubic diamond in addition to the dominant *d/h* layer stacking disordered phase revealed by XRD. An additional shoulder near to 1,170 cm^{-1} is observed in grain 6 and in some areas from grain 7 (Fig. 5*C*), the origin of which is unclear (*SI Appendix*, *Supplementary Information 3*). We note that TEM images of grain 7 reveal a graphitic coating (*SI Appendix*, Fig. S4) that could partly give rise to the strong sp^2-bonded Raman

Downloaded from https://www.pnas.org by Universita di Milano Bicocca on July 25, 2022 from IP address 149.132.95.191.

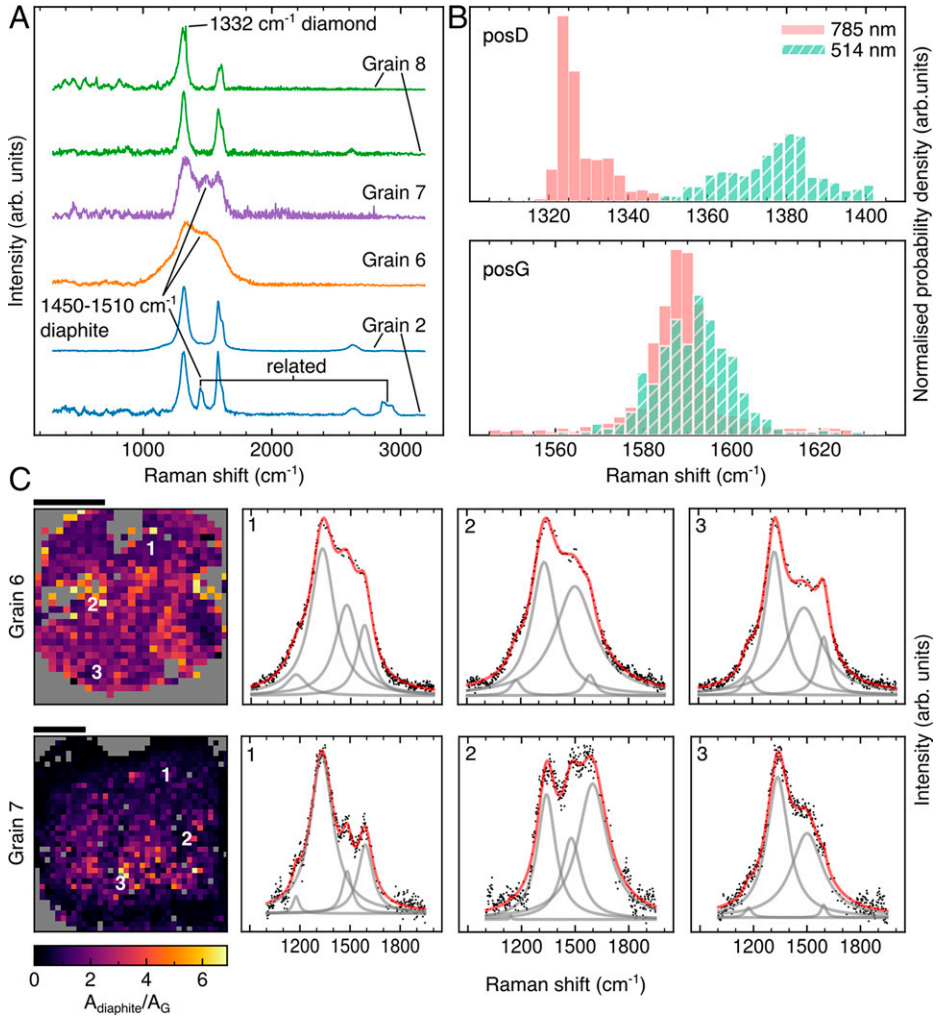

Fig. 5. Raman spectroscopic and mapping data from Canyon Diablo hard carbon grains. (*A*) Representative spectra from grains 2, 6, 7, and 8, including spectra showing the structural variability for grains 2 and 8. The sharp maximum at 1,332 cm^{-1} is due to rare cubic diamond particles distributed within grain 8. (*B*) Histograms of the D and G peak positions in grain 6 with 514.5-nm (green) and 785-nm (red) laser excitation. Here the dispersive nature of the D peak is demonstrated while the position of the G peak remains approximately constant for both wavelengths. (*C*) $A_{diaphite}/A_G$ heat maps of grain 6 and grain 7. The proportion of the diaphite component is estimated from the integrated area contribution of the 1,450- to 1,510- cm^{-1} feature relative to the G peak intensity within the fitted spectra. These maps demonstrate the presence of the diaphite peak across the sample and its intensity relative to the G peak. (Scale bar: 100 μm.)

signatures. Grain 2 is dominated by a graphitic structure containing bundles of 3R stacking (*SI Appendix*, Fig. S4), although regions with sp^3-bonded carbon also occur (*SI Appendix*, Table S2). Its Raman spectra show mainly the characteristic bands for graphitic carbon. The bands for grain 6 are significantly broader than those from grains 7 and 8, which could be associated with the greater degree of nanoscale structural disorder observed by TEM and XRD mapping.

An additional Raman feature occurs between 1,450 and 1,510 cm^{-1}, most prominent in grains 6 and 7, which contain a large proportion of diaphite structures. DFT calculations show that bands in this region are expected to occur for diaphite nanostructures (17) (*SI Appendix*, Fig. S9), and we suggest that the 1,450- to 1,510- cm^{-1} feature observed from grains 6 and 7 is correlated with these nanostructured units. We use this assignment to illustrate the spatial distribution of diaphite structures in terms of heat maps of the relative peak area ($A_{diaphite}/A_G$) of the 1,450- to 1,510- cm^{-1} feature and 1,580- to 1,590- cm^{-1} G bands in the Canyon Diablo samples (Fig. 5*C*). We note that the 1,450- to 1,510- cm^{-1} feature also appears in grain 2, where it coincides with a second-order band at ∼2,900 cm^{-1} that lies close to D+D′ for disordered graphite (Fig. 5*A*). The $A_{diaphite}/A_G$ heat maps show the persistence of this peak across the whole sample areas of both grains 6 and 7, with a stronger signal appearing in grain 6 (Fig. 5*C*). We note that the 1,584- cm^{-1} band can be assigned to the G peak, both of a graphitic phase included in the sample, and of graphene-like domains forming part of the diaphite nanostructures.

Discussion

Our combined synchrotron XRD, HRTEM, and Raman data (Figs. 2–4) show that hard carbon grains from the Canyon Diablo iron meteorite, which have previously been identified as lonsdaleite, are comprised of a mixture of micro- to nanoscale structures containing *c/h* diamond layer stacking, type 1 and 2 diaphite, and graphitic domains. These structures have also been identified throughout natural and synthetic micro- and nanodiamonds found in meteorites and laboratory-synthesized samples (9, 10, 12, 14–17). In fact, we suggest the material interpreted as "lonsdaleite" and reported from various natural and laboratory-prepared samples corresponds to intergrowths of *c/h* stacking disordered diamond and diaphite domains, instead of 2H diamond.

Downloaded from https://www.pnas.org by Universita di Milano Bicocca on July 25, 2022 from IP address 149.132.95.191.

Our multianalytical investigation of the type of material from which "lonsdaleite" was first described (3, 4) provides a solution for resolving the confusion for the name "lonsdaleite," which is used to identify a mineral and a structure. The mineral "lonsdaleite" is characterized by the reported broadened XRD patterns, TEM, and Raman features. However, this material does not possess the ideal, macroscopic 2H stacking pattern. A similar issue arises for "perovskite," in which the mineral perovskite $CaTiO_3$ does not possess the cubic perovskite structure (44). Therefore, we suggest keeping the name "lonsdaleite" for the type specimen in honor of Dame Kathleen Lonsdale, but noting that its structure consists of *c/h* stacking disordered diamond and diaphite. We also propose using the "*c/h* stacked disordered diamond and diaphite" description instead of "lonsdaleite" for interpreting structural features of XRD, TEM, and Raman data. This terminology can be extended to synthetic materials and does not exclude the existence of 2H diamond. In fact, nanosized 2H domains have been reported within hierarchically structured diamond composites (45), but the finding of a bulk material with 2H stacking will be the subject of future studies.

Diaphite nanostructures occupy a wide range of phase space between the sp^3- and sp^2-bonded end members and would be expected to be encountered as intermediates formed by compression or decompression from graphite or diamond, or by metastable synthesis from molecular precursors via chemical or physical vapor deposition (9, 10). In fact, we suggest that diaphite structures should be involved for calculating the energetics of the graphite-to-diamond phase transition (46, 47). As noted above, nanometer-sized diamond domains occur throughout the graphitic matrix (Fig. 3*E*), suggesting that their formation was arrested during an early stage of the graphite-to-diamond transition (48), and that the diamond formation began simultaneously and spontaneously at multiple points throughout the sample. This behavior would be consistent with the system reaching a mechanical instability limit during metastable compression of graphite and beyond the equilibrium graphite–diamond transition, with the observed nanostructures appearing through minimization of the elastic strains associated with diaphite formation (49). However, it was noted from Raman spectroscopy that a few areas within some grains exhibited the characteristic sharp peak of crystalline cubic diamond (Fig. 5*A*), indicating that these had achieved sufficiently high temperature during the shock event to complete the thermodynamic transformation. Barbaro et al. (50–52) found nano- and microdiamonds coexisting with nanographite aggregates in ureilite meteorites and estimated 1,200 to 1,300 °C for this phase assemblage. In accordance with these reports, we hypothesize analogous shock T for the Canyon Diablo sample. The diamond materials within the samples are intimately associated with graphitic structures that could represent the starting phase present within the meteorite sample, possibly formed from exsolution of iron carbide (28, 32), or that could have appeared during the decompression stage immediately following passage of the shock wave.

In addition to the remarkable mechanical properties combining aspects of the extreme compressive strength and tensile resistance of diamond and graphitic intergrowths and nanocomposites, we expect these materials to display desirable electronic properties. Although diamond is a well-known wide-bandgap insulator, it can be made conducting and even superconducting by substitution of B for C atoms within the lattice, or by the introduction of nitrogen-vacancy defects (53). The existence of diaphite structures with a conducting interface between the graphene and diamond layers provide another mechanism for introducing potentially superconducting pathways into the otherwise insulating material (24, 54–56). In order to achieve such sp^2-bonded nanostructures embedded within the diamond matrix in a controllable manner will require development of precise layer-by-layer growth techniques.

Materials and Methods

Samples. Carbonaceous grains from a Canyon Diablo iron meteorite were obtained following the procedure described in ref. 57. The Canyon Diablo samples are from the Buseck Center for Meteorite Studies of Arizona State University. The grains are black with an adamantine luster (*SI Appendix*, Fig. S1), and their size ranged from tens of microns to several millimeters. Some of these grains are soft and graphite-like, while others showed extreme resistance to mechanical abrasion and were classified as "diamonds." From 100 grains four representative grains, 2, 6, 7, and 8 (*SI Appendix*, Fig. S1 and Table S1), were investigated with XRD, TEM, and Raman spectroscopy and mapping.

Microbeam XRD and DIFFaX Modeling. Selected carbonaceous grains from the Canyon Diablo iron meteorite were mounted at the end of glass fibers and studied using a 2 × 2 micrometer X-ray beam ($\lambda = 0.03738$ nm) at the ID27 beamline of the ESRF-EBS synchrotron facility in Grenoble, France. Two-dimensional maps of 36 points in grain 2 and 100 points in grains 6, 7, and 8 were obtained and they were integrated using the Dioptas software (58). Selected maps are shown in Fig. 2. The XRD data were analyzed using the DIFFaX protocol based on models built for sp^3-bonded *c/h* layers and for type 1 and type 2 diaphite structures. Details of the fitting procedure of *c/h* diamond and type 1 diaphite were presented previously (9, 10, 14–16). The analysis of type 2 diaphite is described in *SI Appendix, Supplementary Information 2*.

TEM Investigation and Image Processing. FIB lamellae measuring 10 × 2 μm in area and ∼40 to 50 nm thick were prepared from grains 2, 6, and 7 applying FIB thinning with Thermo Scientific Scios 2 Dual Beam equipment. Aberration-corrected TEM and high-angle annular dark-field scanning TEM images were acquired using a Thermo Fisher Scientific FEI THEMIS 200 microscope (Institute of Technical Physics and Materials Science, Hungary, 200 keV, 0.07-nm point resolution). FFTs were calculated using Gatan Digital Micrograph 3.6.1 software. The amplitude image in Fig. 3*C* was generated from Fig. 3*B* following the method described in Hÿtch et al. (59) using routines written for the Digital Micrograph software and applying 0.06-nm^{-1}-sized Lorentzian masks for the 003 set of 3R graphite reflections of the FFT (Fig. 1*B*). We measured the d-spacings of graphene layers from intensity profiles of FFTs calculated across the 00*l* reflections using Velox software. We note that we use three *hkl* indices for labeling diffraction spots and d-spacings of graphite and four indices *hkil* [$i = -(h + k)$] whenever we discuss crystallographic planes and directions.

Microbeam Raman Spectroscopy and Mapping. Raman maps were acquired for grains 6 and 7 as well as single point spectra for grains 2 and 8 using a Renishaw inVia confocal micro-Raman instrument equipped with 785- and 514.5-nm lasers through an Olympus 50× objective. The laser was focused to ∼3 μm and the power at the sample was maintained at <2 mW for the 10- to 20-s acquisition times. We did not observe any transformation of the samples with these irradiation conditions. The maps were constructed using 810 and 1369 points for grains 6 and 7, respectively, with step sizes of 10 μm. Random spikes due to cosmic rays impacting the detector were removed using a custom method based on that proposed by Whitaker and Hayes (60). The spectra were then background-corrected using a rolling ball filter based on principles set out in ref. 61.

Data Availability. All study data are included in the article and/or supporting information.

ACKNOWLEDGMENTS. We are grateful to Paul F. McMillan for his contribution to help with this work and lasting contributions to the wider field of diamond research. We acknowledge the staff and use of the facilities in the Themis Titan HRTEM facility located at the Institute of Technical Physics and Materials Science, Centre for Energy Research. P.N. and Z.F. acknowledge financial support from the Hungarian National Research, Development and Innovation Office

Downloaded from https://www.pnas.org by Universita di Milano Bicocca on July 25, 2022 from IP address 149.132.95.191.

project NKFIH_KH126502 and the János Bolyai Research Scholarship. B.P. acknowledges support of the projects VEKOP-2.3.3-15-2016-00002 and TKP2021-NKTA-05. L.A.J.G. was supported by NASA Emerging Worlds grant NNX17AE56G. P.F.M., C.A.H., and F.C. received funding from the EU Graphene Flagship under Horizon 2020 Research and Innovation program grant agreements 785219-GrapheneCore2 and 881603-GrapheneCore3. R.L.S. received a DTP studentship from the University College London (UCL) Department of Chemistry. M.Murri received support from the Barringer Family Fund for Meteorite Impact Research. This work made use of the ARCHER UK National Supercomputing Service (www.archer.ac.uk) via K.M. and F.C.'s membership in the HEC Materials Chemistry Consortium, which is funded by the Engineering and Physical Sciences Research Council (EPSRC) (EP/L000202). K.M. and F.C. gratefully acknowledge HPC resources provided by the UK Materials and Molecular Modelling Hub, which is partially funded by EPSRC (EP/P020194/1), and UCL Grace and Kathleen HPC Facilities and associated support services in completion of this work. We acknowledge the European Synchrotron Radiation Facility for provision of synchrotron beamtime at the beamline ID27.

Author affiliations: [a]Institute for Geological and Geochemical Research, Research Centre for Astronomy and Earth Sciences (MTA Centre of Excellence), Eötvös Loránd Research Network, H-1112 Budapest, Hungary; [b]Department of Physics & Astronomy, University College London, London WC1E 6BT, United Kingdom; [c]Department of Chemistry, University College London, London WC1H 0AJ, United Kingdom; [d]Department of Chemistry, University of Bath, Bath BA2 7AX, United Kingdom; [e]Institute of Technical Physics and Materials Science, Centre for Energy Research (MTA Centre of Excellence), Eötvös Loránd Research Network, H-1121 Budapest, Hungary; [f]Buseck Center for Meteorite Studies, Arizona State University, Tempe, AZ 85287; [g]Department of Earth and Environmental Sciences, University of Milano-Bicocca, 20126 Milano, Italy; and [h]Experiments Division, European Synchrotron Radiation Facility, Grenoble 38000, France

1. F. P. Bundy, J. S. Kasper, Hexagonal diamond – A new form of carbon. *J. Chem. Phys.* **46**, 3437–3446 (1967).
2. G. R. Cowan, B. W. Dunnington, A. H. Holtzman, "Process for synthesizing diamond." US patent 3401019-A (1968).
3. R. E. Hanneman, H. M. Strong, F. P. Bundy, Hexagonal diamonds in meteorites: Implications. *Science* **155**, 995–997 (1967).
4. C. Frondel, U. B. Marvin, Lonsdaleite, a hexagonal polymorph of diamond. *Nature* **214**, 587–589 (1967).
5. C. Le Guillou, J. N. Rouzaud, L. Remusat, A. Jambon, M. Bourot-Denise, Structures, origin and evolution of various carbon phases in the ureilite Northwest Africa 4742 compared with laboratory-shocked graphite. *Geochim. Cosmochim. Acta* **74**, 4167–4185 (2010).
6. V. Kvasnytsya *et al.*, New evidence of meteoritic origin of the Tunguska cosmic body. *Planet. Space Sci.* **84**, 131–140 (2013).
7. F. Nestola *et al.*, Impact shock origin of diamonds in ureilite meteorites. *Proc. Natl. Acad. Sci. U.S.A.* **117**, 25310–25318 (2020).
8. Z. Pan, H. Sun, Y. Zhang, C. Chen, Harder than diamond: Superior indentation strength of wurtzite BN and lonsdaleite. *Phys. Rev. Lett.* **102**, 055503 (2009).
9. P. Németh *et al.*, Diamond-graphene composite nanostructures. *Nano Lett.* **20**, 3611–3619 (2020).
10. P. Németh *et al.*, Complex nanostructures in diamond. *Nat. Mater.* **19**, 1126–1131 (2020).
11. F. Isobe, H. Ohfuji, H. Sumiya, T. Irifune, Nanolayered diamond sintered compact obtained by direct conversion from highly oriented graphite under high pressure and high temperature. *J. Nanomater.* **380136**, (2013).
12. P. Németh *et al.*, Lonsdaleite is faulted and twinned cubic diamond and does not exist as a discrete material. *Nat. Commun.* **5**, 5447 (2014).
13. P. Németh, L. A. J. Garvie, P. R. Buseck, Twinning of cubic diamond explains reported nanodiamond polymorphs. *Sci. Rep.* **5**, 18381 (2015).
14. C. G. Salzmann, B. J. Murray, J. J. Shephard, Extent of stacking disorder in diamond. *Diamond Related Materials* **59**, 69–72 (2015).
15. A. P. Jones *et al.*, Structural characterization of natural diamond shocked to 60 GPa; implications for Earth and planetary systems. *Lithos* **265**, 214–221 (2016).
16. M. Murri *et al.*, Quantifying hexagonal stacking in diamond. *Sci. Rep.* **9**, 10334 (2019).
17. P. Németh *et al.*, Diaphite-structured nanodiamonds with with six- and twelve-fold symmetries. *Diamond Related Materials* **119**, 108573 (2021).
18. P. Németh *et al.*, Impact-formed complex diamond-graphene nanostructures. *Resol. Discov.*, 10.1556/2051.2021.00089.
19. H. Ohnishi, K. Nasu, Generation and growth of sp^3-bonded domains by visible photon irradiation of graphite. *Phys. Rev. B Condens. Matter Mater. Phys.* **80**, 014112 (2009).
20. J. Kanasaki, E. Inami, K. Tanimura, H. Ohnishi, K. Nasu, Formation of sp^3-bonded carbon nanostructures by femtosecond laser excitation of graphite. *Phys. Rev. Lett.* **102**, 087402 (2009).
21. Z. Zhao *et al.*, Coherent interfaces with mixed hybridization govern direct transformation from graphite to diamond. Research Square [Preprint] (2021). 10.21203/rs.3.rs-934066/v1 (Accessed 7 July 2022).
22. K. Luo *et al.*, Novel boron nitride polymorphs with graphite-diamond hybrid structure. *Chin. Phys. Lett.* **39**, 036301 (2022).
23. K. Luo, B. Liu, L. Sun, Z. Zhao, Y. Tian, Design of a class of new sp2–sp3 carbons constructed by graphite and diamond building blocks. *Chin. Phys. Lett.* **38**, 028102 (2021).
24. Y. Ge *et al.* Superconductivity in graphene hybrid. *Mater. Today Phys.* **23**, 100630 (2022).
25. X. Yang *et al.*, Diamond-graphite nanocomposite synthesized from multi-walled carbon nanotubes fibers. *Carbon* **172**, 138–143 (2021).
26. S. Zhang *et al.*, Narrow-gap, semiconducting, superhard amorphous carbon with high toughness, derived from C60 fullerene. *Cell Rep. Phys. Sci.* **2**, 100575 (2021).
27. T. C. Fitzgibbons *et al.*, Benzene-derived carbon nanothreads. *Nat. Mater.* **14**, 43–47 (2015).
28. R. Brett, G. T. Higgins, Cliftonite; a proposed origin, and its bearing on the origin of diamonds in meteorites. *Geochim. Cosmochim. Acta* **33**, 1473–1484 (1967).
29. L. A. J. Garvie, "Observations on a 10-kg graphite nodule from the Canyon Diablo (IAB-MG) iron meteorite" in *47th Lunar and Planetary Science Conference* (LPSC, 2016), **vol. 47**, 2567.
30. C. J. Ksanda, E. P. Henderson, Identification of diamond in the Canyon Diablo iron. *Am. Mineral.* **24**, 677–680 (1939).
31. F. K. Dalton, Microhardness testing of iron meteorites. *J. R. Astron. Soc. Can.* **44**, 1–11 (1950).
32. M. Lipschutz, E. Anders, The record in the meteorites-IV: Origin of diamonds in iron meteorites. *Geochim. Cosmochim. Acta* **24**, 83–105 (1961).
33. G. P. Vdovykin, The Canyon Diablo meteorite. *Space Sci. Rev.* **14**, 758–831 (1973).
34. S. Zhang *et al.*, Ultrastrong p-bonded interface as ductile plastic flow channel in nanostructured diamond. *ACS Appl. Mater. Interfaces* **12**, 4135–4142 (2020).
35. Q. Zhang *et al.*, Designing ultrahard nanostructured diamond through internal defects and interface engineering at different length scales. *Carbon* **170**, 394–402 (2020).
36. A. C. Ferrari, J. Robertson, Raman spectroscopy of amorphous, nanostructured, diamond-like carbon, and nanodiamond. *Philos. Trans.- Royal Soc., Math. Phys. Eng. Sci.* **362**, 2477–2512 (2004).
37. M. A. Pimenta *et al.*, Studying disorder in graphite-based systems by Raman spectroscopy. *Phys. Chem. Chem. Phys.* **9**, 1276–1291 (2007).
38. A. Merlen, J. G. Buijnsters, C. A. Pardanaud, Guide to and review of the use of multiwavelength Raman spectroscopy for characterizing defective aromatic carbon solids: From graphene to amorphous carbons. *Coatings* **7**, 153 (2017).
39. D. B. Schuepfer *et al.*, Assessing the structural properties of graphitic and non-graphitic carbons by Raman spectroscopy. *Carbon* **161**, 359–372 (2020).
40. S. Osswald, V. N. Mochalin, M. Havel, G. Yushin, Y. Gogotsi, Phonon confinement effects in the Raman spectrum of nanodiamond. *Phys. Rev. B Condens. Matter Mater. Phys.* **80**, 075419 (2009).
41. N. N. Ovsyuk, S. V. Goryainov, A. Y. Likhacheva, Raman scattering in hexagonal diamond. *Bull. Russ. Acad. Sci.* **82**, 778–780 (2018).
42. A. C. Ferrari, Raman spectroscopy of graphene and graphite: Disorder, electron–phonon coupling, doping and nonadiabatic effects. *Solid State Commun.* **143**, 47–57 (2007).
43. A. C. Ferrari, D. M. Basko, Raman spectroscopy as a versatile tool for studying the properties of graphene. *Nat. Nanotechnol.* **8**, 235–246 (2013).
44. R. Mitchell, M. D. Welch, A. R. Chakhmouradian, Nomenclature of the perovskite supergroup: A hierarchical system of classification based on crystal structure and composition. *Min. Mag. (Lond.)* **81**, 411–461 (2017).
45. Y. Yue *et al.*, Hierarchically structured diamond composite with exceptional toughness. *Nature* **582**, 370–374 (2020).
46. P. Xiao, G. Henkelman, Communication: From graphite to diamond: Reaction pathways of the phase transition. *J. Chem. Phys.* **137**, 101101 (2012).
47. Y. P. Xie, X. J. Zhang, Z. P. Liu, Graphite to diamond: Origin for kinetics selectivity. *J. Am. Chem. Soc.* **139**, 2545–2548 (2017).
48. L. A. J. Garvie, P. Németh, P. R. Buseck, Transformation of graphite to diamond via a topotactic mechanism. *Am. Mineral.* **99**, 531–538 (2014).
49. D. Machon, F. Meersman, M. C. Wilding, M. Wilson, P. F. McMillan, Pressure-induced amorphization and polyamorphism: Inorganic and biochemical systems. *Prog. Mater. Sci.* **61**, 216–282 (2014).
50. A. Barbaro *et al.*, Graphite based geothermometry on Almahata Sitta ureilites meteorites. *Minerals (Basel)* **10**, 1005 (2020).
51. A. Barbaro *et al.*, Origin of micrometer-sized impact diamonds in ureilites by catalytic growth involving Fe-Ni-silicide: The example of Kenna meteorite. *Geochim. Cosmochim. Acta* **309**, 286–298 (2021).
52. A. Barbaro *et al.*, Characterization of carbon phases in Yamato 74123 ureilite to constrain the meteorite shock history. *Am. Mineral.* **107**, 377–384 (2022).
53. V. N. Mochalin, O. Shenderova, D. Ho, Y. Gogotsi, The properties and applications of nanodiamonds. *Nat. Nanotechnol.* **7**, 11–23 (2011).
54. C. Liu, X. Song, Q. Li, Y. Ma, C. Chen, Superconductivity in compression-shear deformed diamond. *Phys. Rev. Lett.* **124**, 147001 (2020).
55. M. Hu *et al.*, Three-dimensional sp(2)-hybridized carbons consisting of orthogonal nanoribbons of graphene and net C. *Phys. Chem. Chem. Phys.* **17**, 13028–13033 (2015).
56. X. Wang *et al.*, The microscopic diamond anvil cell: Stabilization of superhard, superconducting carbon allotropes at ambient pressure. arXiv [Preprint] (2022). https://arxiv.org/abs/2204.03231 (Accessed 7 July 2022).
57. L. A. J. Garvie, P. Németh, "The structure of Canyon Diablo diamonds" in *40th Lunar and Planetary Science Conference* (LPSC, 2009), **vol. 40**, 1346.
58. C. Prescher, V. B. Prakapenka, DIOPTAS: A program for reduction of two-dimensional X-ray diffraction data and data exploration. *High Press. Res.* **35**, 223–230 (2015).
59. M. J. Hÿtch, E. Snoeck, R. Kilaas, Quantitative measurement of displacement and strain fields from HREM micrographs. *Ultramicroscopy* **74**, 131–146 (1998).
60. D. A. Whitaker, K. Hayes, A simple algorithm for despiking Raman spectra. *Chemom. Intell. Lab. Syst.* **179**, 82–84 (2018).
61. I. K. Mikhailyuk, A. P. Razzhivin, Background subtraction in experimental data arrays illustrated by the example of Raman spectra and fluorescent gel electrophoresis patterns. *Instrum. Exp. Tech.* **46**, 765–769 (2003).

Downloaded from https://www.pnas.org by Universita di Milano Bicocca on July 25, 2022 from IP address 149.132.95.191.